Journal of Energy Storage 63 (2023) 106958

Contents lists available at ScienceDirect

Journal of Energy Storage

journal homepage: www.elsevier.com/locate/est

Research papers

Thermochemical energy storage using calcium magnesium acetates under low CO_2 pressure conditions

Nabil Amghar [a], Pedro E. Sánchez Jiménez [a,b,*], Luis A. Pérez Maqueda [a,**], Antonio Perejón [a,b,*]

[a] Instituto de Ciencia de Materiales de Sevilla (C.S.I.C.-Universidad de Sevilla), C. Américo Vespucio 49, 41092 Sevilla, Spain
[b] Departamento de Química Inorgánica, Facultad de Química, Universidad de Sevilla, 41012 Sevilla, Spain

ARTICLE INFO

Keywords:
Concentrated solar power
Calcium-magnesium acetates
Thermochemical energy storage
Calcium-looping
Low CO_2 pressure

ABSTRACT

The calcium looping multicycle performance of CaO-based materials, derived from calcium magnesium acetates with different Mg content were tested under experimental conditions compatible with thermochemical energy storage. In order to reduce the sintering-induced decay in performance, calcination at an absolute CO_2 pressure of 0.1 bar and 0.01 bar is implemented. CaO carbonation is performed at standard 1 bar CO_2 conditions. The samples can be fully calcined in short residence times. Samples with MgO present high cycling stability, even when the MgO content is as low as 5 mol%. The effective conversion values lie within the range 0.88–0.84 over ten calcination/carbonation cycles, which provides an accumulated energy storage density of 90.9 GJ/m^3. This outstanding reactivity is related with the microstructure of the sample after calcination composed of CaO nanoparticles that are highly reactive for carbonation.

1. Introduction

Improving the deployment and efficiency of renewable energies is currently the most viable solution towards the aim of global decarbonization. Among renewable energies, concentrated solar power (CSP), which exploits the energy from the sun to generate electricity, has attracted a lot of attention in terms of investment and research in the last decades. Thus, a total of 135 concentrated solar power projects have been under operation, construction or development from 2006 to 2021 around the world in 10 countries [1]. They contribute to mitigate the environmental impact related to electricity production, as the massive reduction in CO_2 emissions is one of the main worldwide challenge nowadays [2,3]. However, this challenge can only be met if the problem of direct solar radiation variability is addressed through the development of low-cost solar energy storage technologies based on abundant, non-toxic materials that enable the commercial expansion of solar energy on a large scale [4–6].

Currently, molten salts (mixtures of $NaNO_3/KNO_3$) are used as sensible heat thermal energy storage system integrated in the first and second generation concentrated solar power (CSP) plants [7,8]. It is, therefore, a mature technology that allows decoupling production and demand [8]. However, molten salts present serious limitations related to their cost, corrosiveness, the maximum operation temperatures (~560 °C to avoid degradation) and the requirement of storing them at temperatures over 220 °C to avoid their solidification, which penalize the CSP plant performance [9–13]. Next generation of CSP plants contemplate operation at temperatures over 600 °C, which would significantly boost the power-to-heat efficiency [14,15]. Furthermore, storage concepts with higher energy densities are under consideration. Thermochemical energy storage (TCES), while still in the research and development phase, has great potential. It is based on the heat exchanged in reversible chemical reactions, which inherently high enthalpies result in very high energy densities [16–19]. The integration of a TCES system in a CSP plant is devised as follows; the heat generated by concentrated solar power is used to carry out the endothermic chemical reaction whose products would be stored separately. When energy demand requires it, the reverse exothermic reaction is carried out and the stored heat released to produce energy. The capability for long-term storage of the reaction products without thermal losses is another advantage of TCES systems over concepts that rely on latent or sensible heat storage [20–23].

Several thermochemical energy storage systems have been proposed, such as redox reactions of metallic oxides, ammonia decomposition, hydration/dehydration reactions, sulphur cycles and carbonation/

* Corresponding authors at: Instituto de Ciencia de Materiales de Sevilla (C.S.I.C.-Universidad de Sevilla), C. Américo Vespucio 49, 41092 Sevilla, Spain.
** Corresponding author.
E-mail addresses: pedro.enrique@icmse.csic.es (P.E. Sánchez Jiménez), maqueda@cica.es (L.A. Pérez Maqueda), aperejon@us.es (A. Perejón).

https://doi.org/10.1016/j.est.2023.106958
Received 26 July 2022; Received in revised form 27 January 2023; Accepted 22 February 2023
Available online 11 March 2023

decarbonation reactions [22,24,25]. Among the latter, extensive research has been devoted to the calcium looping (CaL) process for thermochemical energy storage in CSP plants, due to the high theoretical energy storage density of $CaCO_3$/CaO, 4.82 GJ/(m^3 $CaCO_3$), which corresponds to a value of 10.62 GJ/(m^3 CaO) if the calcined solid is considered in the calculations [26–32]. The CaL-CSP integration consists in using the concentrated solar energy on a bed or stream of $CaCO_3$ to induce its calcination at high temperature (about 750 °C in inert gas or 950 °C in CO_2) [33–37]. The reaction products, CaO and CO_2, are transported out of the calciner and stored separately. When demand requires energy production, these products are brought back together in the carbonator to carry out the exothermic carbonation reaction to regenerate the $CaCO_3$. As the process can be carried out at temperatures as high as 800 °C [33,38], gas turbines could be used for electricity production with higher efficiency than the steam turbines used in conventional CSP plants [39–41]. Another advantage of the CaL process is that CaO could be exploited in other industrial applications requiring heat [38,42].

However, the CaL technology presents some drawbacks for its integration in CSP plants, mainly the high temperature needed to carry out the calcination reaction, which promotes the progressive sintering-induced deactivation of CaO along the carbonation and calcination cycles [34,43,44]. Previous results from theoretical models and numerical simulations estimate that stable sorbent conversion values above 20 % are required for CaL-CSP plants to best the efficiencies currently attained in CSP plant equipped with molten salt storage systems [29].

Two main general approaches have been used to enhance the reactivity of CaO during the multiple carbonation/calcination cycles: (i) modifying the operating conditions in terms of temperature and atmosphere in order to attenuate sintering [45–48], and the use of other natural or synthetic Ca-based materials with improved structural stability [49–52]. Among these materials, dolomite, $CaMg(CO_3)_2$, exhibits very stable CaO multicycle performance [53–55] due to the role of inert MgO arising during the first calcination. However, MgO constitutes 41.8 wt% in calcined dolomite, which significantly reduces the maximum attainable energy density. In addition, calcium acetate derived CaO shows promising results as its decomposition leads to highly reactive CaO particles of small size [56,57]. However, the decay in activity is also fast unless structural stability is improved, normally by the use of additives [56].

Regarding the operating conditions, it has been proposed to carry out the calcination under inert gases such as helium, nitrogen or argon, allowing the calcination temperatures to be reduced below 750 °C, according to the thermodynamic equilibrium of the $CaCO_3$/CaO system [27,54,58]. However, the use of an inert gas during calcination entails implementing a costly separation stage that imposes a significant energy penalty on the process [59]. Steam has also proven effective in reducing the calcination temperature as it combines high thermal conductivity and certain catalytic effects promoting the desorption of CO_2 during calcination [60–64]. Another alternative is the operation under a closed CO_2 cycle, in which both carbonation and calcination would be carried out in pure CO_2 atmosphere [27,45]. This permits avoiding gas separation processes or condensation steps but it requires increasing the calcination temperature up to 950 °C in order to achieve the complete calcination of $CaCO_3$ in reasonable residence times. These extreme operating conditions severely deteriorate the multicycle activity of CaO due to extensive sintering and loss of surface area available for carbonation [27,28,45].

Very recently, it has been proposed a new operating scheme that involves calcination at moderate temperatures under low absolute CO_2 pressures (0.1–0.01 bar) and carbonation at high temperatures under CO_2 at atmospheric pressure [46,47]. Previous results have shown these conditions result in notably enhanced reactivity for limestone derived CaO, as compared to previously reported conditions. Thus, it is of the most interest to study the multicycle performance of other CaO-based materials, with inherently better performance under these milder operation conditions. In this work, the reactivity of CaO obtained from dolomite and acetate precursors with different CaO/MgO ratios has been tested.

2. Materials and methods

2.1. Materials

Natural limestone, dolomite and magnesite, provided by Matagallar (Pedrera, Spain), Bueres (Asturias, Spain) and Magnesitas Navarras (Navarra, Spain), respectively, were used in this work. Acetic acid of high purity (99.9 %) from VWR chemicals (CAS: 64-19-7) was used for the synthesis of the acetates.

2.2. Characterization methods

X-ray diffractograms were collected in the 2θ range from 20° to 70° for dolomite and from 5° to 30° for the acetates, using a Rigaku Miniflex diffractometer working at 40 kV and 15 mA. Scanning Electron Microscopy (SEM) was used to study the microstructure of the as prepared and cycled samples. An ultra-high resolution HITACHI S4800 instrument was used. HRTEM and HAADF-STEM micrographs were registered using a Talos F200S FEG microscope. For this purpose, the powder samples were deposited on copper grids.

In situ X-ray diffractograms (XRD) during the calcination process were acquired in vacuum using a powder diffractometer (Bruker D8 Advance) fitted with a high-temperature chamber (Anton Paar XRK 900) and a fast response/high sensitivity detector (Bruker Vantec 1). The temperature during the in situ XRD experiment was increased at 10 °C/min from 400 °C up to 750 °C. XRD scans of 295 s were recorded in the range of $20° < 2\theta < 60°$ (0.03° per step), each 25 °C. Scans were all registered at constant temperature. The BET surface areas and total pore volumes (determined from the N_2 absorbed at $p/p_0 = 0.99$) of the samples were measured in an ASAP2420 Micromeritics instrument. The samples were degassed at 400 °C in vacuum for 2 h and then measured at a temperature of −196 °C.

2.3. Synthesis of the CaO-based materials

Magnesite and limestone were calcined in air in a furnace at 800 °C for 2 h in order to obtain the corresponding calcium and magnesium oxides. Three acetates with different Ca/Mg molar ratios were prepared: calcium acetate (CaAc) using calcined limestone (CaO) as a precursor, Ca80Mg20Ac using a mixture of calcined limestone and calcined magnesite (MgO) in a molar ratio of 80%CaO/20%MgO, and Ca95Mg05Ac from a mixture in a molar ratio of 95%CaO/5%MgO. For the synthesis of each acetate, 1 g of the mixtures of CaO and MgO were treated with 50 mL of an aqueous solution of acetic acid (25 % in volume), and stirred for 2 h at room temperature. Then, the solution was dried at 120 °C for approximately 2 h to obtain the calcium and magnesium acetate crystals. Further details can be found in [56]. Table 1 includes the molar and mass ratio of CaO and MgO corresponding to the four samples used in this work.

Fig. 1 shows the XRD patterns of the four samples studied in this work. From this data, the dolomite sample is a phase pure material, as

Table 1
Molar and mass ratio of CaO and MgO for the four samples used in this work. The theoretical densities of the corresponding calcined materials are also included.

Sample	CaO (mol%)	MgO (mol%)	CaO (mass%)	MgO (mass%)	ρ calcined (kg/m^3)
Dolomite	50	50	58.2	41.8	3440
CaAc	100	0	100	0	3340
Ca80Mg20Ac	80	20	84.8	15.2	3377
Ca95Mg05Ac	95	5	96.4	3.6	3349

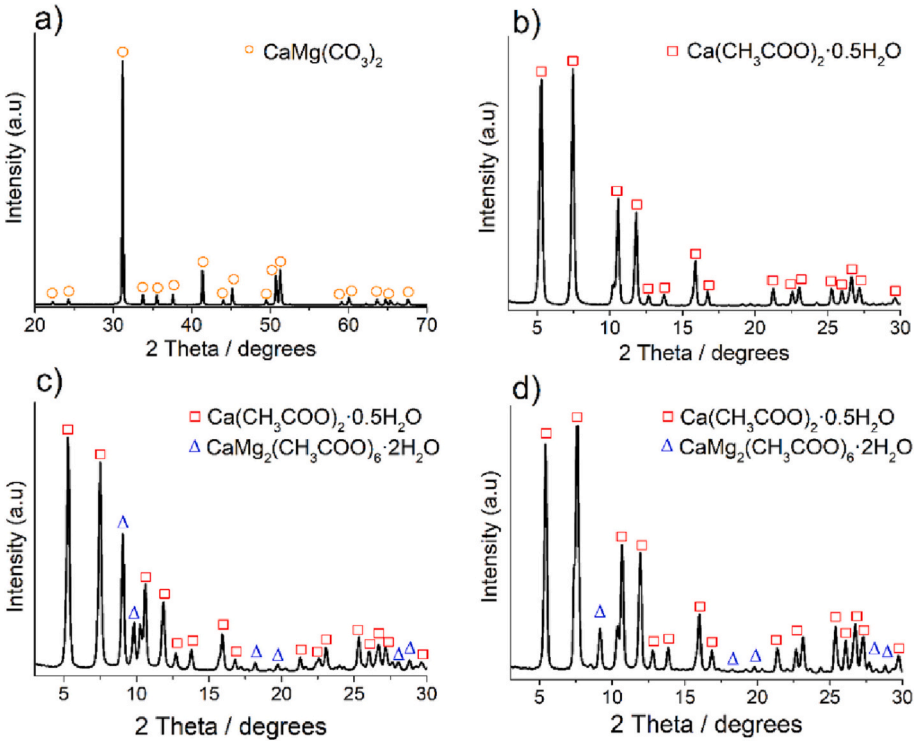

Fig. 1. XRD patterns of (a) dolomite, and the different acetates prepared in this work: (b) CaAc, (c) Ca80Mg20Ac and (d) Ca95Mg05Ac.

well as the CaAc sample, composed only of hydrated calcium acetate. On the other hand, Ca80Mg20Ac and Ca95Mg05Ac are composed of a mixture of calcium acetate and calcium magnesium acetate in different proportions, with no other crystalline phases. From the intensity of the XRD peaks, a higher amount of calcium magnesium acetate was detected for Ca80Mg20Ac, which is consistent with the relative amounts of calcium oxide and magnesium oxide used as precursors.

Fig. 2 shows the representative SEM images of dolomite (Fig. 2a) and Ca95Mg05Ac (Fig. 2b). Dolomite is composed of platelets, while Ca95Mg05Ac presents an acicular morphology, which is typical of the acetates, with a particle size in the range 200–150 μm. Moreover, the microstructure and particle size of the acetate is maintained after decomposition to the carbonate (Fig. 2c) and to the oxides (Fig. 2d). The same particle sizes were obtained for CaAc and Ca80Mg20Ac.

2.4. *Multicycle experiments*

Multicycle experiments were performed in an in-house

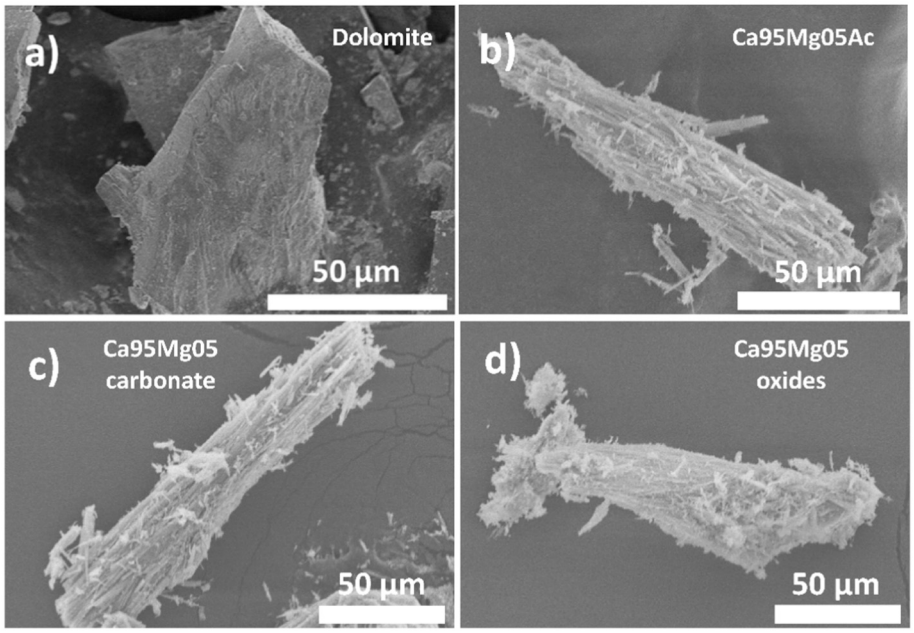

Fig. 2. SEM micrographs of (a) dolomite, (b) Ca95Mg05Ac, (c) Ca95Mg05Ac after decomposition to the carbonate, and (d) Ca95Mg05Ac after decomposition to the oxides.

thermogravimetric instrument prepared to work from low pressures (0.01 bar) up to 5 bar. Fig. 3 shows a scheme of the instrument. It consists of a microbalance and a reactor composed of a furnace and a non-porous mullite tube. A flat crucible was used to hold the sample in the microbalance in order to facilitate the contact of the sample with the gases. The CO_2 pressure was controlled by means of a vacuum pump, a pressure gauge and a pressure measurement system. Further details of the instrument can be found in [46,65].

The multicycle calcination/carbonation tests were performed using 40 mg of the samples in all cases, operating in a closed CO_2 cycle in which absolute pressures of 0.01 bar and 0.1 bar CO_2 were employed for calcination. The calcination temperatures were 700 °C and 760 °C respectively, selected according to the thermodynamic equilibrium of the $CaCO_3$/CaO system [66,67] and in order to optimize the multicycle performance of the materials at different temperatures attainable by conventional solar receivers [68].

An absolute pressure of 1 bar CO_2 was used for carbonation in all tests, at 700 °C, 760 °C and 850 °C. Table 2 summarizes the operating conditions tested in this work.

Prior to the start of the multicycle tests, the system was stabilized at the selected absolute CO_2 pressure, using the vacuum pump. Then, the calcination stage was started by increasing linearly the temperature up to the corresponding calcination temperature, which was hold for 10 min to ensure a complete calcination. Then, the temperature was changed to the carbonation temperature. Once the temperature was stable, the vacuum pump was disconnected and the CO_2 pressure was then increased to 1 bar to initiate the carbonation reaction, lasting 10 min. At that point, the temperature was again decreased to the calcination temperature for a new cycle. Heating and cooling rates of 10 °C/min were always employed.

The multicycle performance of the samples was evaluated by means of the effective conversion, defined as the mass ratio of calcium oxide converted in the carbonation stage at each N-cycle to the total mass of the sample before carbonation (m_i), including solids inert to carbonation. The term $m_{carb}(t) - m_i$ is therefore the CO_2 uptake ($m_{CO_2}(t)$) in each cycle:

$$X_{eff} = \frac{(m_{carb}(t) - m_i)}{m_i}\frac{W_{CaO}}{W_{CO_2}} = \frac{m_{CO_2}(t)}{m_i}\frac{W_{CaO}}{W_{CO_2}} \quad (1)$$

The terms W_{CaO} and W_{CO_2} are the molar masses of CaO and CO_2, respectively. It is important to remark that the effective conversion takes into account the presence of solids that are inert to carbonation under the experimental conditions used in this work. This parameter is more interesting for practical purposes than the CaO conversion, since the inert solids will be also circulated through the system and will influence the efficiency of the process. From Eq. (1), the energy storage capacity (D_m) of the tested materials in kJ/kg for each cycle can be quantified using Eq. (2):

$$D_m = \frac{m_{CO_2}(t)\cdot\Delta H_R}{m_i} \quad (2)$$

where m_{CO_2} is CO_2 uptake during carbonation, as stated above, and ΔH_R is the enthalpy of the reaction (4045.5 kJ/kg CO_2). The energy storage density (D_v) in GJ/m^3 was obtained by multiplying the energy storage capacity and the density of the calcined materials in kg/m^3 (Eq. (3)):

$$D_v = D_m \times \rho \quad (3)$$

As a first approximation, the theoretical densities of the calcined materials were considered for the calculations of D_v, included in Table 1.

Table 2
Operating conditions used for calcination and carbonation. The acronyms have been used to identify the experimental conditions in the text.

Test	Calcination		Carbonation	
	Temperature, °C	Absolute CO_2 pressure, bar	Temperature, °C	Absolute CO_2 pressure, bar
E1	700	0.01	700	1
E2			760	1
E3			850	1
E4	760	0.1	760	1
E5			850	1

3. Results and discussion

3.1. Multicycle activity

Fig. 4 shows, as an example, the evolution of the effective conversion during 10 calcination/carbonation cycles as a function of time for a test E2 on the sample Ca80Mg20Ac, in which calcination was performed at

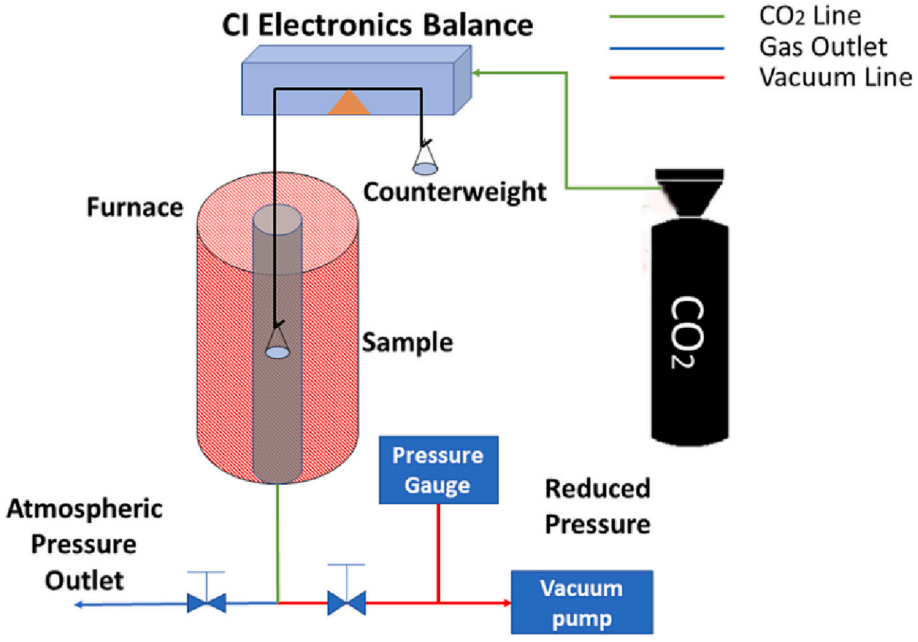

Fig. 3. Scheme of the in-house thermogravimetric instrument used in this work.

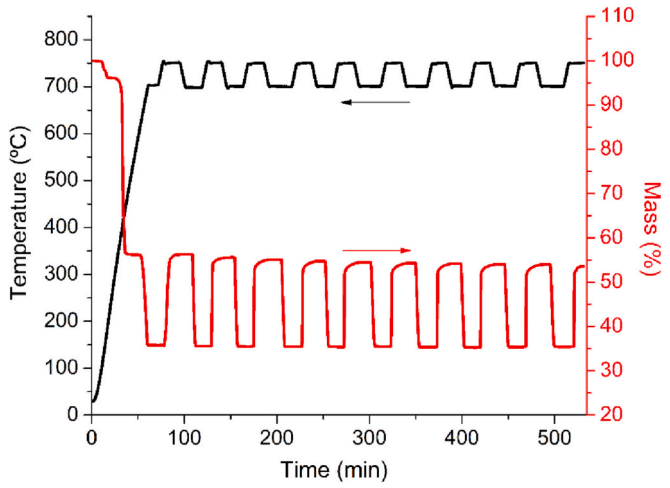

Fig. 4. Time evolution of the mass and temperature for the sample Ca80Mg20Ac, measured during calcination/carbonation cycles under experimental conditions E2.

700 °C and 0.01 bar CO_2, whereas calcination was carried out at 760 °C and 1 bar CO_2 (Table 2). In the first calcination, three mass losses are observed, ascribed to dehydration, decomposition of the acetate to obtain the carbonate, and finally the subsequent decomposition of the carbonate to yield CaO. From this point, the successive CaO carbonation and $CaCO_3$ calcination stages alternated. As may be observed, under the calcination conditions corresponding to test E2, fast calcinations and carbonations were attained. The mass gain was similar in each carbonation stage, which is an indication of a stable multicycle performance.

Fig. 5 shows the values of effective conversion at the end of carbonation as a function of the cycle number for the four samples tested in this work, under the five type of tests included in Table 2. The theoretical maximum effective conversion values are also included as horizontal lines in the figure for comparison purposes (X_{eff} max). For each sample, similar conversion values were obtained regardless the performed test, with the exception of CaAc, that presented a more obvious decrease in effective conversion with the cycle number for the experiment E3.

These results are in contrast with those presented for natural limestone, with a particle size in the range 160–200 μm, tested under similar conditions, in which the reactivity strongly depends on the absolute CO_2 pressure used for calcination and the temperature of carbonation [46].

Table 3 includes the values of effective conversion in the first ($X_{eff}(1)$) and tenth cycle ($X_{eff}(10)$) for all the test carried out, and the differences between them, expressed as ΔX_{eff}. It can be observed that ΔX_{eff} values are higher for dolomite and CaAc than for the magnesium calcium acetates.

The low values of effective conversion attained for dolomite (Fig. 5a), as compared with the rest of samples, are due to the presence of MgO (1 mol per mol of CaO) on the calcined sample that is inert to carbonation under the experimental conditions used in this work. The amount of MgO in calcined dolomite is approximately 42 wt%. For this reason, the maximum value of effective conversion attainable for dolomite is 0.58. It has been amply demonstrated that the MgO grains

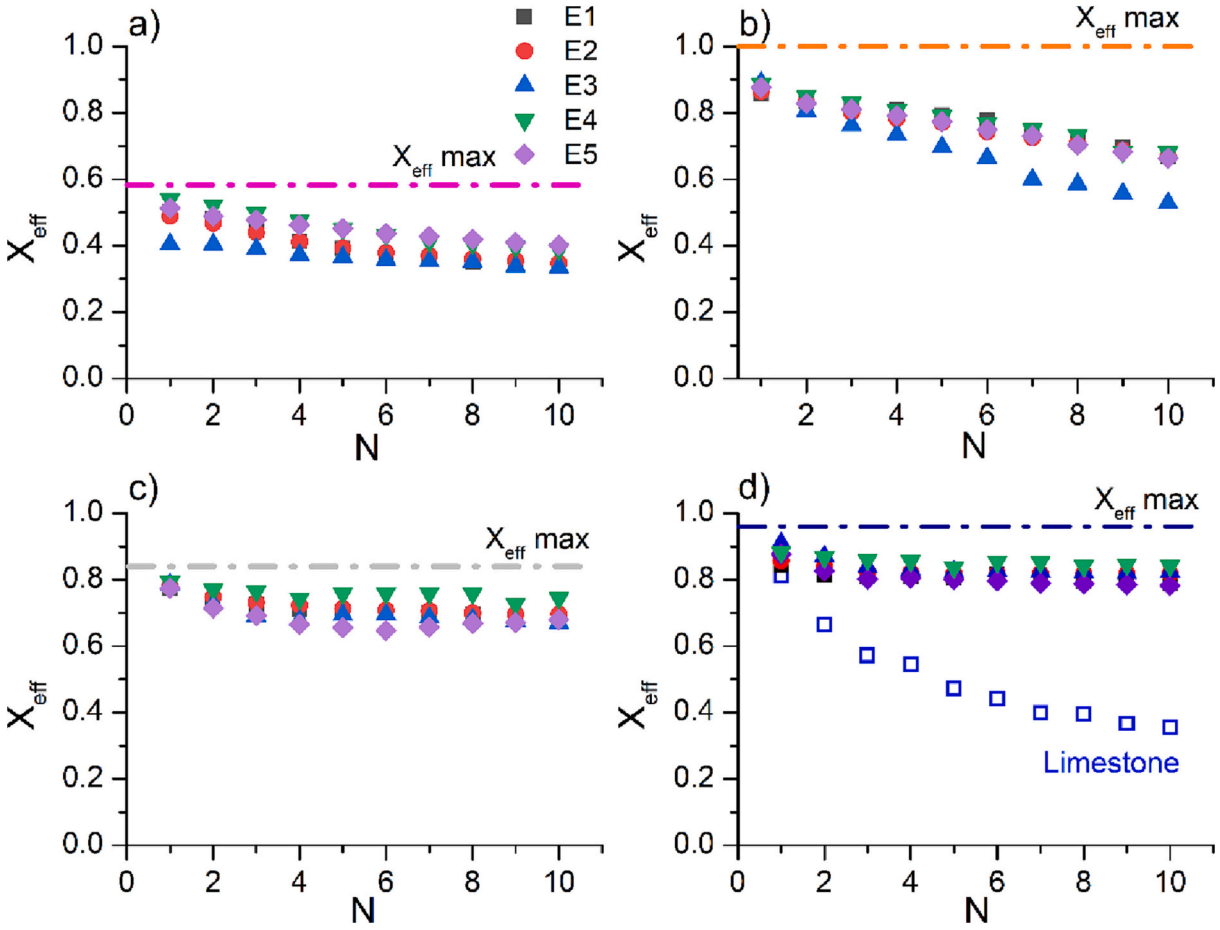

Fig. 5. Effective conversion as a function of the cycle number measured for the four samples studied in this work, tested under experimental conditions E1–E5: (a) dolomite; (b) CaAc; (c) Ca80Mg20Ac; (d) Ca95Mg05Ac. The X_{eff} values of limestone calcined at 765 °C under 0.1 bar CO_2 and carbonated at the same temperature at an absolute pressure of 1 bar CO_2 is also included for comparison.

Table 3
Effective conversion in the first and tenth cycle, and the difference between them (ΔX_{eff}) for the four samples studied in this work under experimental conditions E1–E5.

Test	Sample	$X_{eff}(1)$	$X_{eff}(10)$	ΔX_{eff}
E1	Dolomite	0.50	0.34	−0.16
E2		0.49	0.35	−0.14
E3		0.40	0.34	−0.06
E4		0.54	0.39	−0.15
E5		0.51	0.40	−0.11
E1	CaAc	0.86	0.67	−0.19
E2		0.86	0.67	−0.19
E3		0.89	0.53	−0.36
E4		0.89	0.68	−0.21
E5		0.88	0.66	−0.22
E1	Ca80Mg20Ac	0.77	0.68	−0.09
E2		0.78	0.70	−0.08
E3		0.79	0.67	−0.12
E4		0.79	0.74	−0.05
E5		0.77	0.68	−0.09
E1	Ca95Mg05Ac	0.84	0.79	−0.05
E2		0.86	0.82	−0.04
E3		0.90	0.83	−0.08
E4		0.88	0.84	−0.04
E5		0.88	0.78	−0.10

hampers the sintering of CaO-based materials during the carbonation/calcination cycles, which explains the stable effective conversion attained for dolomite [54,69,70]. Thus, ΔX_{eff} is in the range from −0.11 to −0.16, depending on the test.

In CaAc (Fig. 5b), the calcined sample is composed only of CaO and serves as a reference of a sample with no MgO addition. The values of effective conversion in the first cycle ($X_{eff}(1)$) are obviously much higher than that of dolomite, but, in contrast, the decay in reactivity is significant as can be observed from the values of ΔX_{eff} (Table 3). It has been previously observed that the CaO obtained from the decomposition of CaAc is very reactive to carbonation, but at the expense of intense sintering-induced deactivation in the presence of CO_2 [56,71,72]. As compared to CaAc, the Ca80Mg20Ac sample (Fig. 5c) presents only slightly smaller initial values of $X_{eff}(1)$, attributed to its 20 % molar content of MgO. This corresponds to a mass percentage of 15.2 % in MgO, which is inert to carbonation and thereby reduce the maximum X_{eff} attainable. However, the deactivation along the calcination/carbonation cycles is almost completely suppressed, as can be inferred from the values of ΔX_{eff}, independently of the type of test carried out.

Taking into account the promising results obtained for Ca80Mg20Ac, a sample with even lower content in MgO was prepared, Ca95Mg05Ac. The aim was to reduce the load of inert MgO while still preserving its stabilizing role. The sample was cycled under the all test conditions (E1–E5). As may be seen in Fig. 5d, very high and stable values of effective conversion were obtained during 10 cycles regardless the test performed, with $X_{eff}(1)$ in the range 0.84–0.90 and $X_{eff}(10)$ above 0.78. This material presents an outstanding multicycle performance with ΔX_{eff} of −0.04 for tests E2 and E4. For tests E3 and E5, in which carbonations were carried out at 850 °C, the values of ΔX_{eff} are −0.08 and −0.10, respectively. The effective conversion of natural limestone, calcined at 765 °C under 0.1 bar CO_2 and carbonated at the same temperature at an absolute pressure of 1 bar CO_2 is also included for comparison [46]. A marked decrease on the effective conversion is observed with the cycle number for limestone, in contrast with Ca95Mg05Ac.

In order to assess the influence of the composition on carbonation kinetics, Fig. 6 compares the effective conversion obtained for different samples during the first 90 s of carbonation, those comprising the most relevant part of the carbonation process: the fast reaction-controlled phase. In the subsequent diffusion-controlled phase, the conversion of CaO into $CaCO_3$ is characterized by very slow kinetics [73]. This is clear in Fig. 6, where a sharp increase of the mass in very short times can be observed, followed by the plateau. Carbonation profiles recorded on the

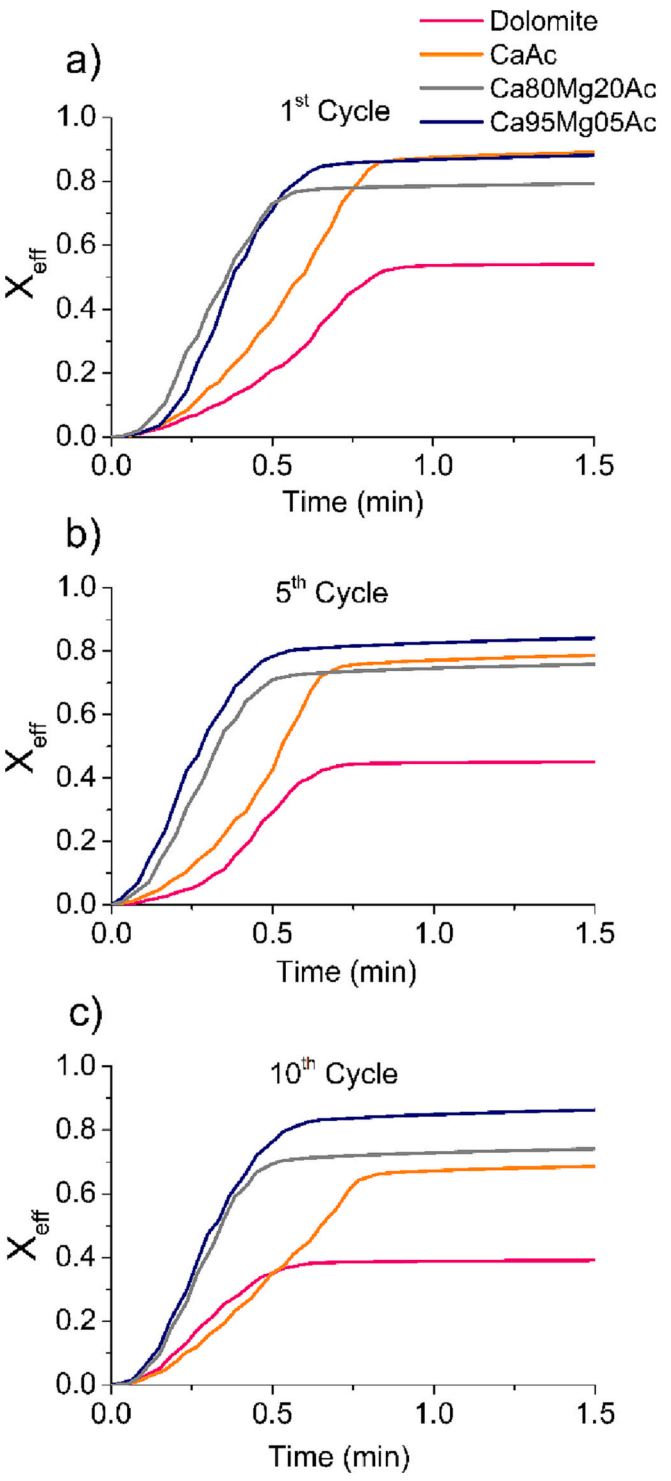

Fig. 6. Effective conversion during the first 90 s of carbonation at the first, fifth and tenth cycle for the samples tested under experimental conditions E4.

first, fifth and tenth carbonation stage are compared to evaluate any changes produced due to the repeating carbonation and calcination cycles. The tests were carried out under experimental conditions E4, but similar behavior was observed in tests run under the experimental conditions corresponding to E1–E5. It is concluded that, although the carbonation rate is not significantly affected by the cycles, it is higher for the MgO-containing samples.

Considering carbonations take place in the fast reaction-controlled phase, the characterization of the surface area (BET) and the pore

volume (V_p) of the samples after calcination was performed in order to correlate the reactivity with the microstructure. The surface area and the pore volume of the samples after a first calcination under experimental conditions E4 (0.1 bar CO_2) are shown in Table 4. The samples present relatively similar surface areas and pore volumes after calcination. The addition of magnesium helps to increase the surface area of the calcined sample, which would be available for carbonation in a high concentration of CO_2.

Fig. 7 presents the values of accumulated energy storage density (D_v), calculated as the sum of D_v for the ten cycles carried out under experimental conditions E4. The value of D_v for limestone is also included, calculated from the data presented in Fig. 5d [46].

As may be seen, dolomite, due to its high content in MgO, has the lower accumulated D_v, but it is just slightly smaller than that of limestone. This again demonstrates how MgO hinders the sintering of the CaO grains, improving its reactivity for carbonation.

Calcium acetate shows a similar value of accumulated D_v than Ca80Mg20Ac despite the decrease in effective conversion of calcium acetate with the cycle number (Fig. 5b). This is because the effective conversion for calcium acetate is very high in the first cycles, giving rise to high values of D_v according to Eq. (3).

On the other hand, Ca95Mg05Ac presents the highest accumulated D_v, since the effective conversion of this sample is in the range 0.88–0.84 over the ten cycles (Fig. 5d). Thus, D_v in the tenth cycle is as high as 9 GJ/m^3. Interestingly, accumulated D_v for Ca95Mg05Ac increases up to approximately 70 % with respect to limestone.

3.2. In-situ X-ray diffraction and microstructural analysis

Considering the results presented above, which demonstrate the outstanding multicycle performance of Ca95Mg05Ac, a microstructural and in-situ X-Ray diffraction analysis was performed in this sample. Fig. 8 presents the in-situ XRD diffractograms measured from 400 °C to 750 °C in vacuum, in order to get a grip on the structural transformations experienced for Ca95Mg05Ac during calcination. Note that the decomposition of the calcium magnesium acetate (deacetylation) to give the mixture of $CaCO_3$ and MgO is not considered, since the products (water and acetone) may damage the device. As expected, at 400 °C, $CaCO_3$ is the main compound. Diffraction peaks corresponding to MgO are under detection limits due to its small molar amount in the sample. As the temperature increases, the diffraction peaks of $CaCO_3$ decrease in intensity and those of CaO become noticeable from 525 °C. At 600 °C, CaO is already the main compound and $CaCO_3$ diffraction peaks are almost negligible. Moreover, at this temperature, the main reflection of MgO at $2\theta = 43°$ starts to appear, albeit weakly. At 625 °C, the sample is only composed of CaO and MgO, which is in agreement with the thermodynamic equilibrium of the $CaCO_3$/CaO system [66,67].

Fig. 9a and b show the micrographs of the Ca95Mg05Ac sample after a first calcination at 0.1 bar CO_2. It may be seen that the microstructure drastically changes after the acetate decomposition, and consists of small CaO grains that are aggregated and mixed with the MgO grains. Fig. 9c, d and e present the EDX analysis of the sample subjected to 10 calcination/carbonation cycles, ending in calcination, performed under experimental conditions E4. It is well-known that the MgO grains, which hamper the aggregation and sintering of the CaO grains, eventually segregate from the CaO matrix during the calcination/carbonation cycles, which gives place to a loss of CaO reactivity as the number of cycles

Table 4
Surface area and pore volume of the samples after calcination at 0.1 bar CO_2.

Sample	S_{BET} (m^2/g)	V_p (cm^3/g)
Dolomite	30.2	0.135
CaAc	20	0.084
Ca80Mg20Ac	29.7	0.121
Ca95Mg05Ac	24.7	0.111

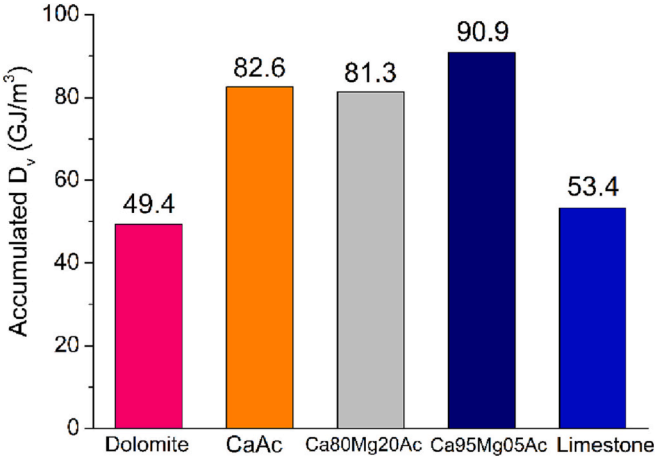

Fig. 7. Accumulated D_v for dolomite, CaAc, Ca80Mg20Ac and Ca95Mg05Ac. The value for limestone is also included, calculated from the data reported in [46].

increases. Some segregation of the MgO grains in Ca95Mg05Ac subjected to 10 cycles is clear in Fig. 9d–e, although it is still well dispersed in some areas of the sample, which justifies the high effective conversion values obtained (Figs. 5–6).

Further insights about the microstructure of the sample were obtained by the transmission electron microscopy analysis, as shown in Figs. 10 and 11. Fig. 10a–d illustrate HRTEM micrographs of Ca95Mg05Ac after the first calcination at 0.1 bar CO_2. It is confirmed that the sample is composed of nanometric CaO grains aggregated in particles of several microns. The grain size is in the order of 100 nm and the MgO grains are much smaller. Fig. 10e–h present HRTEM the micrographs of the sample subjected to 10 calcination/carbonation cycles ending in calcination. As expected, the microstructure changes in such a way that CaO grain size looks more heterogeneous and increases, due to sintering. The small spots seen in Fig. 10e–h may be attributed to MgO segregated from the CaO matrix.

Fig. 11 shows the HRTEM micrographs and the corresponding HAADF-STEM mappings of Ca95Mg05Ac subjected to a first calcination (Fig. 11a–d) and subjected to 10 calcination/carbonation cycles (Fig. 11e–h). The HAADF-STEM mappings of the sample after the first calcination illustrate a homogeneous distribution of the MgO nanograins in the CaO matrix. On the other hand, segregation and aggregation of the MgO nanograins is evident in Fig. 11f, which are located in the CaO grain boundaries. This justifies again the small decrease in reactivity on this sample along the cycles (Figs. 5–6).

4. Conclusions

The CaL multicycle performance of CaO-based materials, obtained of the decomposition of dolomite and calcium-magnesium acetate, has been studied under reaction conditions involving calcination under an absolute CO_2 pressure of 0.1 bar or 0.01 bar and carbonation under 1 bar CO_2. These conditions imply lower calcination temperatures that minimize the sintering-induced deactivation of CaO. At absolute CO_2 pressures of 0.01 bar and 0.1 bar, the starting carbonates can be fully calcined in short residence times at 700 °C or 760 °C, respectively. Furthermore, the nascent CaO particles obtained under these calcination conditions are nanometric size and highly reactive towards subsequent carbonation. Different temperatures were studied for carbonation (700 °C, 760 °C and 850 °C) as depending on the calcination temperatures, to obtain the five types of operating conditions explored. In all cases, CaO carbonation takes place in <1 min, which is a very relevant result for the practical application of the process.

Samples with different MgO content were tested under these novel

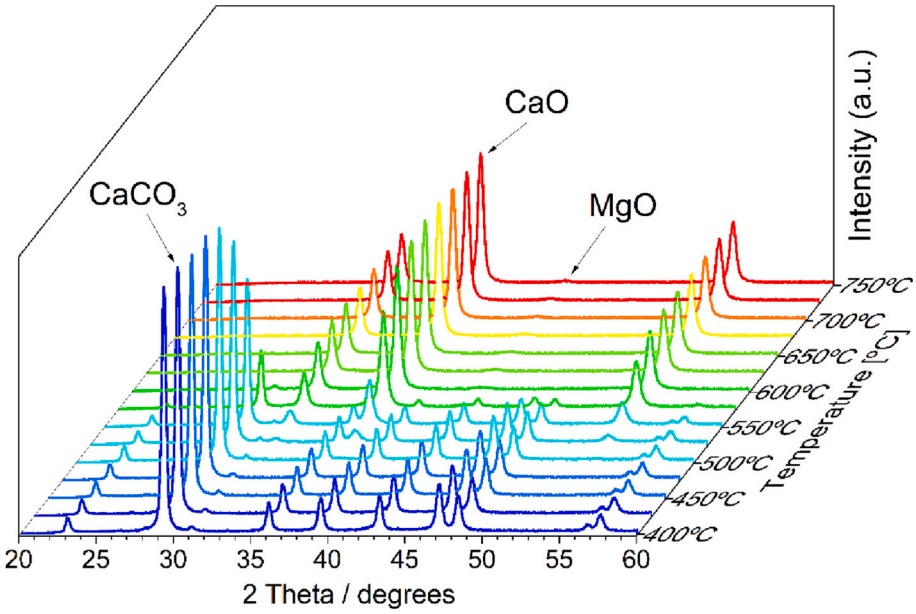

Fig. 8. In-situ XRD patterns of Ca95Mg05Ac, measured from 400 °C to 750 °C in vacuum.

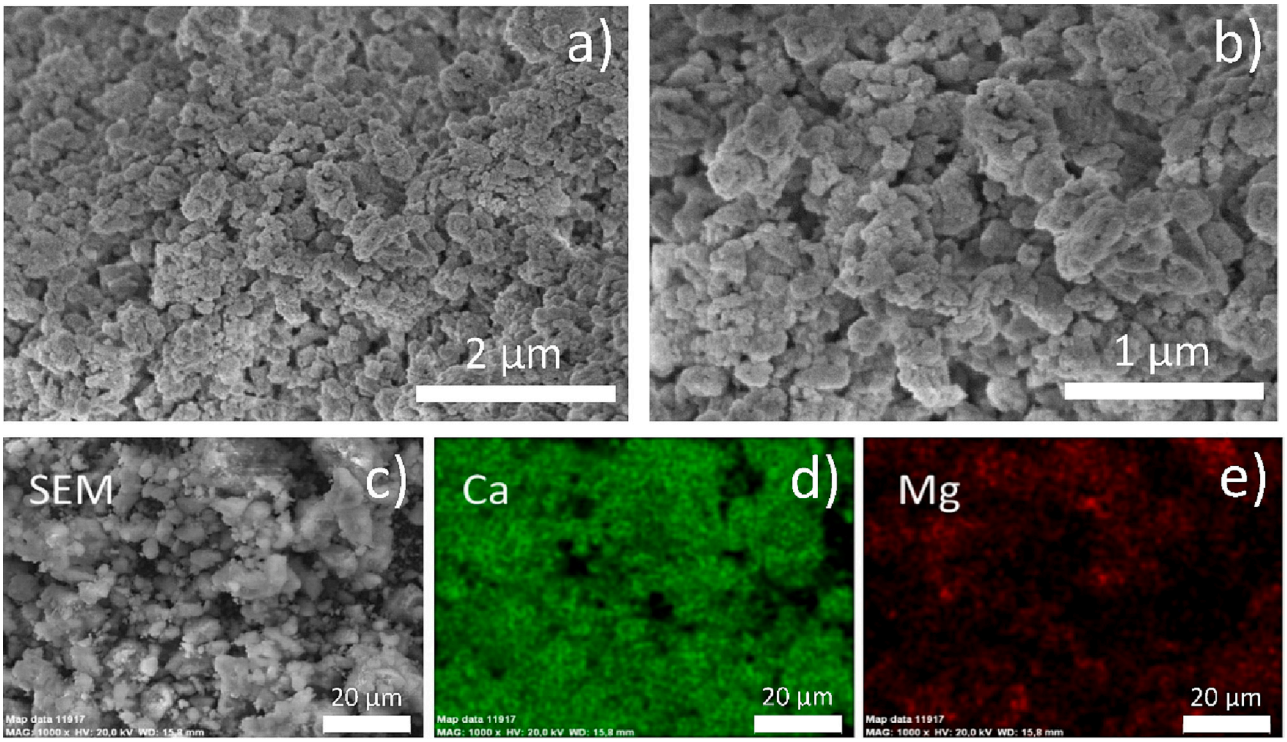

Fig. 9. (a, b) SEM micrographs of Ca95Mg05Ac after a first calcination at 0.1 bar CO_2. (c, d, e) EDX analysis of the sample subjected to 10 calcination/carbonation cycles, ending in calcination.

process conditions. Overall, high cycling stability for the active materials was achieved, save for the CaAc samples that show a slight decay trend due to the absence of MgO which proves very effective in avoiding the CaO deactivation. The accumulated energy density of the sample derived from the calcium-magnesium acetate Ca95Mg05Ac is higher than that of dolomite, CaAc and Ca80Mg20Ac. In particular, Ca95Mg05Ac presents an exceptional multicycle performance even after subjected to 10 calcination/carbonation cycles, which yields an accumulated energy storage density of 90.9 GJ/m^3. It is demonstrated by surface area measurements, SEM and TEM that the excellent results of Ca95Mg05Ac are related with the microstructure of the sample after calcination, and that just 5 mol% addition of MgO is enough to prevent a marked sintering of the CaO grains.

The significant reduction of the calcination temperature and the avoidance of gas separation systems makes this CaL concept attractive for thermochemical energy storage applications.

CRediT authorship contribution statement

Nabil Amghar: Investigation, Writing – original draft, Data curation.

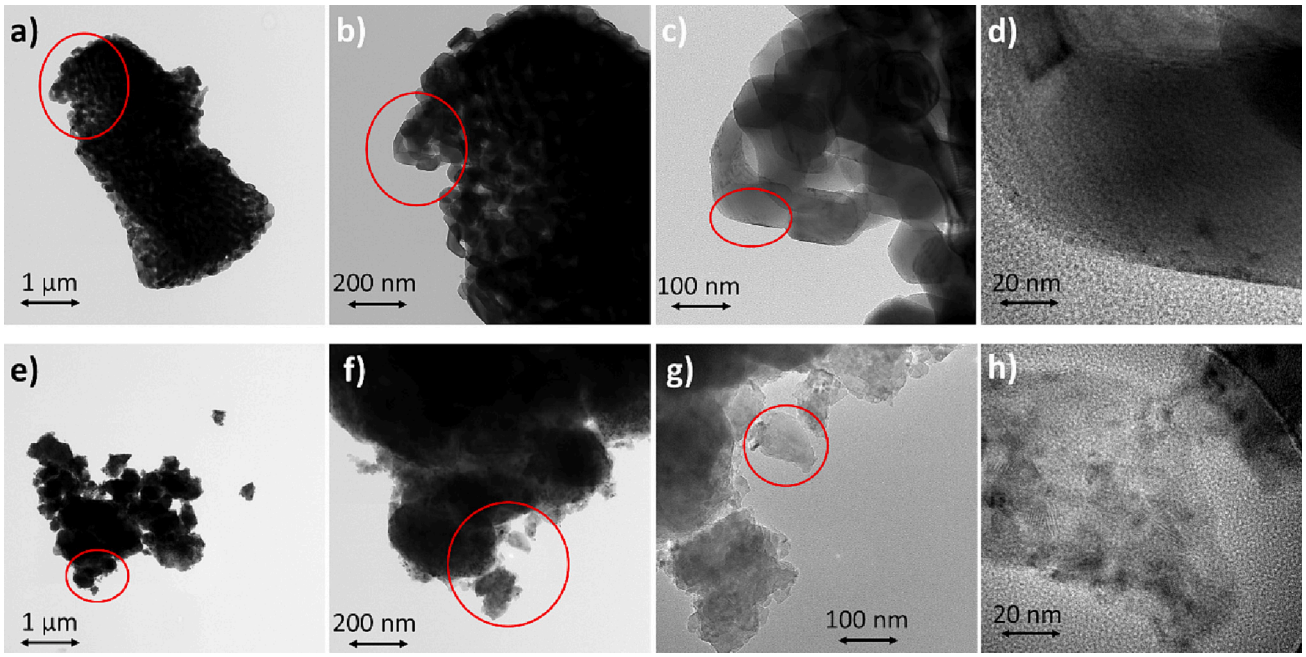

Fig. 10. HRTEM micrographs of Ca95Mg05Ac: (a–d) after calcination at 0.1 bar CO_2; (e–h) subjected to 10 calcination/carbonation cycles ending in calcination.

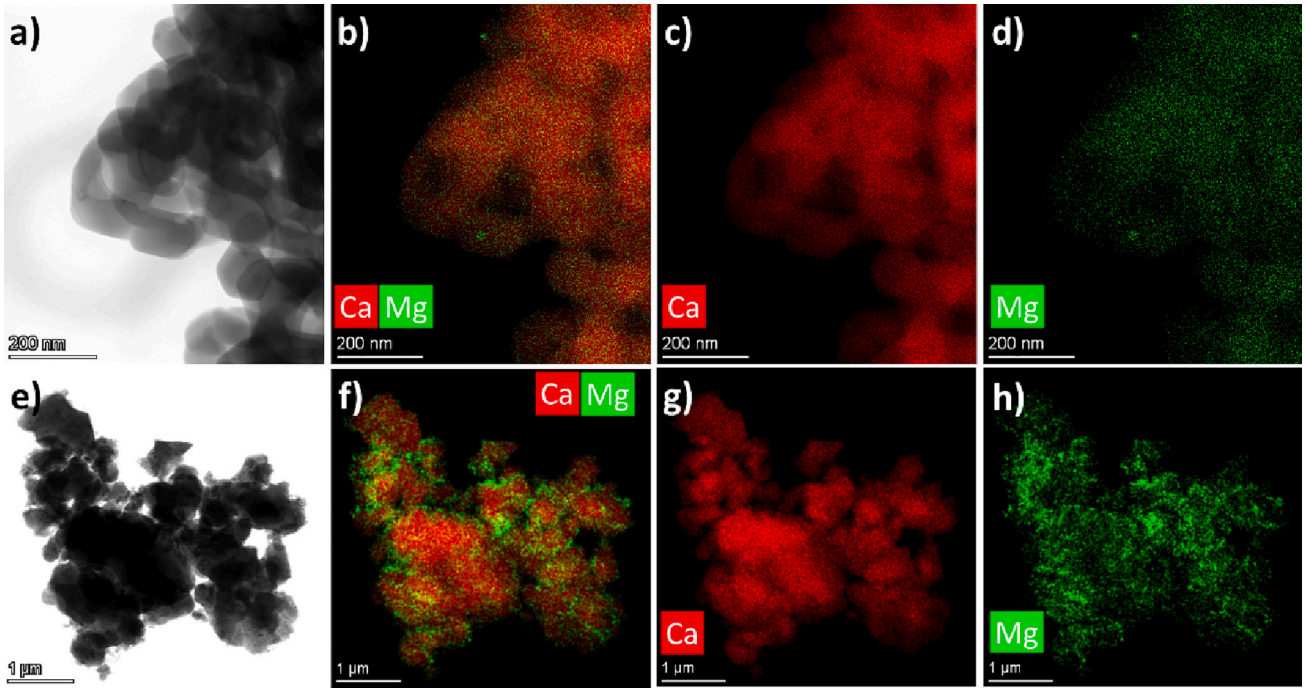

Fig. 11. HRTEM micrographs and HAADF-STEM mappings of Ca95Mg05Ac: (a–d) after calcination at 0.1 bar CO_2; (e–h) subjected to 10 calcination/carbonation cycles ending in calcination.

Pedro E. Sánchez Jiménez: Conceptualization, Writing – review & editing, Supervision. **Luis A. Pérez Maqueda:** Conceptualization, Writing – review & editing, Project administration. **Antonio Perejón:** Investigation, Writing – review & editing, Supervision.

Declaration of competing interest

The authors declare that they have no known competing financial interests or personal relationships that could have appeared to influence the work reported in this paper.

Data availability

Data will be made available on request.

Acknowledgements

This work has been funded by EU Next Generation funds and Spanish Ministry of Science and Innovation (projects TED2021-131839B-C22 and PDC2021-121552-C21), and by the grant CTQ2017-83602-C2-1-R (MCIN/AEI/10.13039/501100011033 and ERDF A way of making

Europe by the European Union).

References

[1] A. Palacios, C. Barreneche, M.E. Navarro, Y. Ding, Thermal energy storage technologies for concentrated solar power – a review from a materials perspective, Renew. Energy 156 (2020) 1244–1265, https://doi.org/10.1016/j.renene.2019.10.127.

[2] M.T. Huang, P.M. Zhai, Achieving Paris Agreement temperature goals requires carbon neutrality by middle century with far-reaching transitions in the whole society, Adv. Clim. Chang. Res. 12 (2) (2021) 281–286, https://doi.org/10.1016/j.accre.2021.03.004.

[3] L.T. Keyßer, M. Lenzen, 1.5 °C degrowth scenarios suggest the need for new mitigation pathways, Nat. Commun. 12 (1) (2021) 2676, https://doi.org/10.1038/s41467-021-22884-9.

[4] S. Kuravi, J. Trahan, D.Y. Goswami, M.M. Rahman, E.K. Stefanakos, Thermal energy storage technologies and systems for concentrating solar power plants, Prog. Energy Combust. Sci. 39 (4) (2013) 285–319, https://doi.org/10.1016/j.pecs.2013.02.001.

[5] G. Alva, L. Liu, X. Huang, G. Fang, Thermal energy storage materials and systems for solar energy applications, Renew. Sust. Energ. Rev. 68 (2017) 693–706, https://doi.org/10.1016/j.rser.2016.10.021.

[6] Y. Tian, C.Y. Zhao, A review of solar collectors and thermal energy storage in solar thermal applications, Appl. Energy 104 (2013) 538–553, https://doi.org/10.1016/j.apenergy.2012.11.051.

[7] G. Gasa, C. Prieto, A. Lopez-Roman, L.F. Cabeza, Life cycle assessment (LCA) of a concentrating solar power (CSP) plant in tower configuration with different storage capacity in molten salts, J. Energy Storage 53 (2022), 105219, https://doi.org/10.1016/j.est.2022.105219.

[8] M.T. Islam, N. Huda, A.B. Abdullah, R. Saidur, A comprehensive review of state-of-the-art concentrating solar power (CSP) technologies: current status and research trends, Renew. Sust. Energ. Rev. 91 (2018) 987–1018, https://doi.org/10.1016/j.rser.2018.04.097.

[9] A. Bonk, S. Sau, N. Uranga, M. Hernaiz, T. Bauer, Advanced heat transfer fluids for direct molten salt line-focusing CSP plants, Prog. Energy Combust. Sci. 67 (2018) 69–87, https://doi.org/10.1016/j.pecs.2018.02.002.

[10] F. Zaversky, J. García-Barberena, M. Sánchez, D. Astrain, Transient molten salt two-tank thermal storage modeling for CSP performance simulations, Sol. Energy 93 (2013) 294–311, https://doi.org/10.1016/j.solener.2013.02.034.

[11] A.G. Fernández, B. Muñoz-Sánchez, J. Nieto-Maestre, A. García-Romero, High temperature corrosion behavior on molten nitrate salt-based nanofluids for CSP plants, Renew. Energy 130 (2019) 902–909, https://doi.org/10.1016/j.renene.2018.07.018.

[12] C. Villada, A. Toro, F. Bolívar, Corrosion performance of austenitic stainless steel SS304 in molten nitrate salts and Raman microscopy for stability analysis in thermal energy storage applications, J. Energy Storage 44 (2021), 103465, https://doi.org/10.1016/j.est.2021.103465.

[13] A.G. Fernández, L.F. Cabeza, Corrosion evaluation of eutectic chloride molten salt for new generation of CSP plants. Part 2: materials screening performance, J. Energy Storage 29 (2020), 101381, https://doi.org/10.1016/j.est.2020.101381.

[14] G. Mohan, M.B. Venkataraman, J. Coventry, Sensible energy storage options for concentrating solar power plants operating above 600 °C, Renew. Sust. Energ. Rev. 107 (2019) 319–337, https://doi.org/10.1016/j.rser.2019.01.062.

[15] J.M. Yin, Q.Y. Zheng, Z.R. Peng, X.R. Zhang, Review of supercritical CO_2 power cycles integrated with CSP, Int. J. Energy Res. 44 (3) (2020) 1337–1369, https://doi.org/10.1002/er.4909.

[16] L. André, S. Abanades, Recent advances in thermochemical energy storage via solid–gas reversible reactions at high temperature, Energies 13 (22) (2020) 5859, https://doi.org/10.3390/en13225859.

[17] L.F. Cabeza, A. Solé, C. Barreneche, Review on sorption materials and technologies for heat pumps and thermal energy storage, Renew. Energy 110 (2017) 3–39, https://doi.org/10.1016/j.renene.2016.09.059.

[18] A. Bayon, R. Bader, M. Jafarian, L. Fedunik-Hofman, Y. Sun, J. Hinkley, S. Miller, W. Lipiński, Techno-economic assessment of solid–gas thermochemical energy storage systems for solar thermal power applications, Energy 149 (2018) 473–484, https://doi.org/10.1016/j.energy.2017.11.084.

[19] N. Yu, R.Z. Wang, L.W. Wang, Sorption thermal storage for solar energy, Prog. Energy Combust. Sci. 39 (5) (2013) 489–514, https://doi.org/10.1016/j.pecs.2013.05.004.

[20] C. Prieto, P. Cooper, A.I. Fernández, L.F. Cabeza, Review of technology: thermochemical energy storage for concentrated solar power plants, Renew. Sust. Energ. Rev. 60 (2016) 909–929, https://doi.org/10.1016/j.rser.2015.12.364.

[21] X. Chen, Z. Zhang, C. Qi, X. Ling, H. Peng, State of the art on the high-temperature thermochemical energy storage systems, Energy Convers. Manag. 177 (2018) 792–815, https://doi.org/10.1016/j.enconman.2018.10.011.

[22] J. Sunku Prasad, P. Muthukumar, F. Desai, D.N. Basu, M.M. Rahman, A critical review of high-temperature reversible thermochemical energy storage systems, Appl. Energy 254 (2019) 113733, https://doi.org/10.1016/j.apenergy.2019.113733.

[23] M. Liu, N.H. Steven Tay, S. Bell, M. Belusko, R. Jacob, G. Will, W. Saman, F. Bruno, Review on concentrating solar power plants and new developments in high temperature thermal energy storage technologies, Renew. Sust. Energ. Rev. 53 (2016) 1411–1432, https://doi.org/10.1016/j.rser.2015.09.026.

[24] Y. Zhang, R. Wang, Sorption thermal energy storage: concept, process, applications and perspectives, Energy Storage Mater. 27 (2020) 352–369, https://doi.org/10.1016/j.ensm.2020.02.024.

[25] A.J. Carrillo, J. González-Aguilar, M. Romero, J.M. Coronado, Solar energy on demand: a review on high temperature thermochemical heat storage systems and materials, Chem. Rev. 119 (7) (2019) 4777–4816, https://doi.org/10.1021/acs.chemrev.8b00315.

[26] G. Flamant, D. Hernandez, C. Bonet, J.P. Traverse, Experimental aspects of the thermochemical conversion of solar energy; decarbonation of CaCO3, Sol. Energy 24 (4) (1980) 385–395, https://doi.org/10.1016/0038-092X(80)90301-1.

[27] R. Chacartegui, A. Alovisio, C. Ortiz, J.M. Valverde, V. Verda, J.A. Becerra, Thermochemical energy storage of concentrated solar power by integration of the calcium looping process and a CO_2 power cycle, Appl. Energy 173 (2016) 589–605, https://doi.org/10.1016/j.apenergy.2016.04.053.

[28] C. Ortiz, J.M. Valverde, R. Chacartegui, L.A. Perez-Maqueda, P. Giménez, The Calcium-Looping (CaCO3/CaO) process for thermochemical energy storage in Concentrating Solar Power plants, Renew. Sust. Energ. Rev. 113 (2019), 109252, https://doi.org/10.1016/j.rser.2019.109252.

[29] S.E.B. Edwards, V. Materić, Calcium looping in solar power generation plants, Sol. Energy 86 (9) (2012) 2494–2503, https://doi.org/10.1016/j.solener.2012.05.019.

[30] S. Pascual, P. Lisbona, M. Bailera, L.M. Romeo, Design and operational performance maps of calcium looping thermochemical energy storage for concentrating solar power plants, Energy 220 (2021), 119715, https://doi.org/10.1016/j.energy.2020.119715.

[31] C. Tregambi, F. Di Lauro, F. Montagnaro, P. Salatino, R. Solimene, 110th anniversary: calcium looping coupled with concentrated solar power for carbon capture and thermochemical energy storage, Ind. Eng. Chem. Res. 58 (47) (2019) 21262–21272, https://doi.org/10.1021/acs.iecr.9b03083.

[32] C. Tregambi, P. Bareschino, E. Mancusi, F. Pepe, F. Montagnaro, R. Solimene, P. Salatino, Modelling of a concentrated solar power – photovoltaics hybrid plant for carbon dioxide capture and utilization via calcium looping and methanation, Energy Convers. Manag. 230 (2021), 113792, https://doi.org/10.1016/j.enconman.2020.113792.

[33] A. Alovisio, R. Chacartegui, C. Ortiz, J.M. Valverde, V. Verda, Optimizing the CSP-calcium looping integration for thermochemical energy storage, Energy Convers. Manag. 136 (2017) 85–98, https://doi.org/10.1016/j.enconman.2016.12.093.

[34] M. Benitez-Guerrero, B. Sarrion, A. Perejon, P.E. Sanchez-Jimenez, L.A. Perez-Maqueda, J. Manuel Valverde, Large-scale high-temperature solar energy storage using natural minerals, Sol. Energy Mater. Sol. Cells 168 (Supplement C) (2017) 14–21, https://doi.org/10.1016/j.solmat.2017.04.013.

[35] A.A. Khosa, T. Xu, B.Q. Xia, J. Yan, C.Y. Zhao, Technological challenges and industrial applications of CaCO3/CaO based thermal energy storage system – a review, Sol. Energy 193 (2019) 618–636, https://doi.org/10.1016/j.solener.2019.10.003.

[36] T. Esence, E. Guillot, M. Tessonneaud, J.L. Sans, G. Flamant, Solar calcination at pilot scale in a continuous flow multistage horizontal fluidized bed, Sol. Energy 207 (2020) 367–378, https://doi.org/10.1016/j.solener.2020.06.098.

[37] T. Esence, H. Benoit, D. Poncin, M. Tessonneaud, G. Flamant, A shallow cross-flow fluidized-bed solar reactor for continuous calcination processes, Sol. Energy 196 (2020) 389–398, https://doi.org/10.1016/j.solener.2019.12.029.

[38] C. Ortiz, M.C. Romano, J.M. Valverde, M. Binotti, R. Chacartegui, Process integration of calcium-looping thermochemical energy storage system in concentrating solar power plants, Energy 155 (2018) 535–551, https://doi.org/10.1016/j.energy.2018.04.180.

[39] C. Ortiz, R. Chacartegui, J.M. Valverde, A. Alovisio, J.A. Becerra, Power cycles integration in concentrated solar power plants with energy storage based on calcium looping, Energy Convers. Manag. 149 (2017) 815–829, https://doi.org/10.1016/j.enconman.2017.03.029.

[40] E. Karasavvas, K.D. Panopoulos, S. Papadopoulou, S. Voutetakis, Energy and exergy analysis of the integration of concentrated solar power with calcium looping for power production and thermochemical energy storage, Renew. Energy 154 (2020) 743–753, https://doi.org/10.1016/j.renene.2020.03.018.

[41] X. Chen, X. Jin, X. Ling, Y. Wang, Indirect integration of thermochemical energy storage with the recompression supercritical CO_2 Brayton cycle, Energy 209 (2020), 118452, https://doi.org/10.1016/j.energy.2020.118452.

[42] C. Tregambi, F. Montagnaro, P. Salatino, R. Solimene, A model of integrated calcium looping for CO_2 capture and concentrated solar power, Sol. Energy 120 (2015) 208–220, https://doi.org/10.1016/j.solener.2015.07.017.

[43] A.A. Scaltsoyiannes, A.A. Lemonidou, On the factors affecting the deactivation of limestone under calcium looping conditions: a new comprehensive model, Chem. Eng. Sci. 243 (2021), 116797, https://doi.org/10.1016/j.ces.2021.116797.

[44] M. Benitez-Guerrero, J.M. Valverde, P.E. Sanchez-Jimenez, A. Perejon, L.A. Perez-Maqueda, Multicycle activity of natural CaCO3 minerals for thermochemical energy storage in concentrated solar power plants, Sol. Energy 153 (Supplement C) (2017) 188–199, https://doi.org/10.1016/j.solener.2017.05.068.

[45] B. Sarrión, A. Perejón, P.E. Sánchez-Jiménez, L.A. Pérez-Maqueda, J.M. Valverde, Role of calcium looping conditions on the performance of natural and synthetic Ca-based materials for energy storage, J. CO2 Util. 28 (2018) 374–384, https://doi.org/10.1016/j.jcou.2018.10.018.

[46] B. Sarrión, A. Perejón, P.E. Sánchez-Jiménez, N. Amghar, R. Chacartegui, J. Manuel Valverde, L.A. Pérez-Maqueda, Calcination under low CO_2 pressure enhances the calcium looping performance of limestone for thermochemical energy storage, Chem. Eng. J. 417 (2021) 127922, https://doi.org/10.1016/j.cej.2020.127922.

[47] C. Ortiz, A. Carro, R. Chacartegui, J.M. Valverde, A. Perejón, P.E. Sánchez-Jiménez, L.A. Pérez-Maqueda, Low-pressure calcination to enhance the calcium

looping process for thermochemical energy storage, J. Clean. Prod. 363 (2022), 132295, https://doi.org/10.1016/j.jclepro.2022.132295.
[48] B. Sarrion, P.E. Sanchez-Jimenez, A. Perejon, L.A. Perez-Maqueda, J.M. Valverde, Pressure effect on the multicycle activity of natural carbonates and a Ca/Zr composite for energy storage of concentrated solar power, ACS Sustain. Chem. Eng. 6 (6) (2018) 7849–7858, https://doi.org/10.1021/acssuschemeng.8b00981.
[49] J. Obermeier, K.G. Sakellariou, N.I. Tsongidis, D. Baciu, G. Charalambopoulou, T. Steriotis, K. Müller, G. Karagiannakis, A.G. Konstandopoulos, A. Stubos, W. Arlt, Material development and assessment of an energy storage concept based on the CaO-looping process, Sol. Energy 150 (2017) 298–309, https://doi.org/10.1016/j.solener.2017.04.058.
[50] K.G. Sakellariou, G. Karagiannakis, Y.A. Criado, A.G. Konstandopoulos, Calcium oxide based materials for thermochemical heat storage in concentrated solar power plants, Sol. Energy 122 (2015) 215–230, https://doi.org/10.1016/j.solener.2015.08.011.
[51] M. Benitez-Guerrero, J.M. Valverde, A. Perejon, P.E. Sanchez-Jimenez, L.A. Perez-Maqueda, Low-cost Ca-based composites synthesized by biotemplate method for thermochemical energy storage of concentrated solar power, Appl. Energy 210 (2018) 108–116, https://doi.org/10.1016/j.apenergy.2017.10.109.
[52] L. Yang, G. Huang, Z. Huang, Optimized design of Ca-based thermochemical heat storage materials for concentrated solar power, J. Energy Storage 43 (2021), 103236, https://doi.org/10.1016/j.est.2021.103236.
[53] F. Di Lauro, C. Tregambi, F. Montagnaro, P. Salatino, R. Chirone, R. Solimene, Improving the performance of calcium looping for solar thermochemical energy storage and CO2 capture, Fuel 298 (2021), 120791, https://doi.org/10.1016/j.fuel.2021.120791.
[54] B. Sarrion, J.M. Valverde, A. Perejon, L. Perez-Maqueda, P.E. Sanchez-Jimenez, On the multicycle activity of natural limestone/dolomite for thermochemical energy storage of concentrated solar power, Energy Technol. 4 (8) (2016) 1013–1019, https://doi.org/10.1002/ente.201600068.
[55] T.D. Humphries, K.T. Møller, W.D.A. Rickard, M.V. Sofianos, S. Liu, C.E. Buckley, M. Paskevicius, Dolomite: a low cost thermochemical energy storage material, J. Mater. Chem. A 7 (3) (2019) 1206–1215, https://doi.org/10.1039/c8ta07254j.
[56] P.E. Sánchez Jiménez, A. Perejón, M. Benítez Guerrero, J.M. Valverde, C. Ortiz, L. A. Pérez Maqueda, High-performance and low-cost macroporous calcium oxide based materials for thermochemical energy storage in concentrated solar power plants, Appl. Energy 235 (2019) 543–552, https://doi.org/10.1016/j.apenergy.2018.10.131.
[57] C. Sun, X. Yan, Y. Li, J. Zhao, Z. Wang, T. Wang, Coupled CO_2 capture and thermochemical heat storage of CaO derived from calcium acetate, Greenhouse Gases Sci. Technol. 10 (5) (2020) 1027–1038, https://doi.org/10.1002/ghg.2021.
[58] H. Sun, Y. Li, Z. Bian, X. Yan, Z. Wang, W. Liu, Thermochemical energy storage performances of Ca-based natural and waste materials under high pressure during CaO/CaCO3 cycles, Energy Convers. Manag. 197 (2019), 111885, https://doi.org/10.1016/j.enconman.2019.111885.
[59] C. Ortiz, J.M. Valverde, R. Chacartegui, L.A. Pérez-Maqueda, P. Gimenez-Gavarrell, Scaling-up the calcium-looping process for CO_2 capture and energy storage, KONA Powder Particle J. 38 (2021) 189–208, https://doi.org/10.14356/kona.2021005.
[60] J. Yin, X. Kang, C. Qin, B. Feng, A. Veeraragavan, D. Saulov, Modeling of CaCO3 decomposition under CO_2/H_2O atmosphere in calcium looping processes, Fuel Process. Technol. 125 (2014) 125–138, https://doi.org/10.1016/j.fuproc.2014.03.036.
[61] A. Coppola, E. Gais, G. Mancino, F. Montagnaro, F. Scala, P. Salatino, Effect of steam on the performance of Ca-based sorbents in calcium looping processes, Powder Technol. 316 (2017) 578–584, https://doi.org/10.1016/j.powtec.2016.11.062.
[62] J. Arcenegui-Troya, P.E. Sánchez-Jiménez, A. Perejón, V. Moreno, J.M. Valverde, L.A. Pérez-Maqueda, Kinetics and cyclability of limestone (CaCO3) in presence of steam during calcination in the CaL scheme for thermochemical energy storage, Chem. Eng. J. 417 (2021), 129194, https://doi.org/10.1016/j.cej.2021.129194.
[63] J. Arcenegui-Troya, P.E. Sánchez-Jiménez, A. Perejón, J.M. Valverde, L.A. Pérez-Maqueda, Steam-enhanced calcium-looping performance of limestone for thermochemical energy storage: the role of particle size, J. Energy Storage 51 (2022), 104305, https://doi.org/10.1016/j.est.2022.104305.
[64] M. Silakhori, M. Jafarian, A. Chinnici, W. Saw, M. Venkataraman, W. Lipiński, G. J. Nathan, Effects of steam on the kinetics of calcium carbonate calcination, Chem. Eng. Sci. 246 (2021), 116987, https://doi.org/10.1016/j.ces.2021.116987.
[65] A. Perejón, P.E. Sánchez-Jiménez, J.M. Criado, L.A. Pérez-Maqueda, Development of a high-pressure thermobalance working under constant rate thermal analysis, J. Therm. Anal. Calorim. 142 (3) (2020) 1329–1334, https://doi.org/10.1007/s10973-020-09644-5.
[66] E.H. Baker, The calcium oxide–carbon dioxide system in the pressure range 1—300 atmospheres, J. Chem. Soc. (Resumed) 0 (1962) 464–470, https://doi.org/10.1039/JR9620000464.
[67] F. Garcia-Labiano, A. Abad, L.F. de Diego, P. Gayán, J. Adánez, Calcination of calcium-based sorbents at pressure in a broad range of CO_2 concentrations, Chem. Eng. Sci. 57 (13) (2002) 2381–2393, https://doi.org/10.1016/S0009-2509(02)00137-9.
[68] C.K. Ho, Advances in central receivers for concentrating solar applications, Sol. Energy 152 (2017) 38–56, https://doi.org/10.1016/j.solener.2017.03.048.
[69] P.E. Sánchez-Jiménez, J.M. Valverde, A. Perejón, A. De La Calle, S. Medina, L. A. Pérez-Maqueda, Influence of ball milling on CaO crystal growth during limestone and dolomite calcination: effect on CO_2 capture at calcium looping conditions, Crystal Growth Des. 16 (12) (2016) 7025–7036, https://doi.org/10.1021/acs.cgd.6b01228.
[70] C. Huang, M. Xu, X. Huai, Z. Liu, Hierarchically porous calcium-based composites synthesized by eggshell membrane templating for thermochemical energy storage of concentrated solar power, J. Energy Storage 52 (2022), 104769, https://doi.org/10.1016/j.est.2022.104769.
[71] J. Miranda-Pizarro, A. Perejón, J.M. Valverde, L.A. Pérez-Maqueda, P.E. Sánchez-Jiménez, CO_2 capture performance of Ca-Mg acetates at realistic calcium looping conditions, Fuel 196 (2017) 497–507, https://doi.org/10.1016/j.fuel.2017.01.119.
[72] D.S. Sultan, C.R. Müller, J.S. Dennis, Capture of CO_2 using sorbents of calcium magnesium acetate (CMA), Energy Fuel 24 (6) (2010) 3687–3697, https://doi.org/10.1021/ef100072q.
[73] P.E. Sanchez-Jimenez, J.M. Valverde, L.A. Perez-Maqueda, Multicyclic conversion of limestone at Ca-looping conditions: the role of solid-sate diffusion controlled carbonation, Fuel 127 (2014) 131–140, https://doi.org/10.1016/j.fuel.2013.09.064.